-RESEARCH PAPER-

International Journal of Mining and Geo-Engineering

IJMGE

IJMGE 58-3 (2024) 257-262

DOI: 10.22059/IJMGE.2024.367498.595117

Dyke detection as the main target of groundwater exploration using Magnetometry and Electromagnetic data

Hosseinali Ghari [a, *], Maryam Mahdavi [a]

[a] *Department of Mining and Metallurgical Engineering, Yazd University, Yazd, Iran.*

Article History:

Received: 02 November 2023.

Revised: 03 January 2024.

Accepted: 24 January 2024.

ABSTRACT

Dolerite structures, such as dykes and sills are the main target for groundwater exploration in the Karoo Supergroup area which is the main stratigraphic unit in South Africa. Morgenzon Farm is one of the sites in the Karoo Supergroup, including a dolerite dyke, which is of interest here. The magnetization/susceptibility and resistivity of the dolerite dyke are significantly larger than those of the encompassing sedimentary materials. Therefore, the low induction number electromagnetic (EM-LIN) and magnetometry approaches may be useful for its detection. The EM-LIN is composed of three techniques: EM38, EM31, and EM34, with the latter being manipulated. Since both EM34 and magnetometry inverse problems are linear, a regularized weighted minimum length solution algorithm is utilized for their inverse modelling, but with one main discrepancy: the model weighting function for the magnetometry method is attained from the multiplication of depth weighting and compactness constraints, while the model weighting function is only equal to depth weighting for the EM34 approach. Recovered susceptibility and conductivity sections derived respectively from magnetic and EM34 data sets show high consistency. Inverted models represent a dolerite dyke in the middle of the profile with a depth range of 4 to 15m.

Keywords: *Dyke, EM-LIN, Groundwater, Magnetometry.*

1. Introduction

1.1. Geophysical data combination and Joint interpretation

The goal of geophysicists is to establish a connection between the model parameters $\boldsymbol{m}$ (such as conductivities or susceptibilities) and the collected data $\boldsymbol{d}$ (such as apparent conductivities or magnetic anomaly). In fact, they are attempting to estimate $\boldsymbol{m}$ based on $\boldsymbol{d}$, which is referred to as the inverse problem. There are at least two principal reasons why the inverse model does not provide an accurate representation of the subsurface: I) the non-uniqueness of the inverse solution, which indicates that many models can be inferred from the collected data, and the computed data from these models may fit the measured data very well; II) the fact that the measured data are always corrupted by some noise, which increases the ambiguity of the solution and makes it unstable. Furthermore, I) individual inversion techniques can only partially reveal the distribution of a single physical property, such as conductivity, in the subsurface. This limitation makes it difficult to fully identify subsurface anomalies in many cases. II) However, resistivity-based methods can overcome their respective drawbacks by combining data in different ways. Hence, the amalgamation of diverse geophysical data sets is often inevitable.

Joint interpretation, cooperative/sequential inversion, and joint inversion are the main three strategies to combine geophysical data sets. Joint interpretation involves first obtaining inversions of various geophysical data sets. Subsequently, the interpretation of subsurface targets is conducted using these independent inverse models together with any other accessible data, such as geological information and well logs. The diagram of joint interpretation process is illustrated in figure1. The process of joint interpretation is inherently subjective, meaning that two geophysicists may provide competing conclusions. This is the main drawback of this technique. Nevertheless, this disparity is inconsequential for the majority of situations. Hence, the simultaneous analysis of geophysical data can serve as a dependable approach for interpreting subsurface structures. This has been supported by various studies conducted by Orlando [1], Al Farajat [2], Sultan et al [3], Karavul et al [4], Gambetta et al [5], Zhang et al [6], and Ebrahimi et al [7].

1.2. Magnetometry and EM-LIN approaches and goal of the paper

Magnetometry, a method working based on the susceptibility contrast of subsurface materials, has been used for different geological goals, such as mining exploration [8], archeology [9], hydrocarbon investigation [10], volcanology structure and monitoring [11, 12], groundwater [13], salt dome detection [14], and etc. The magnetic data interpretation is accomplished either by imaging techniques [15-17] or inversion approaches [18, 19] which the latter is of interest here. Two principal goals of the magnetic data interpretation are the determination of spatial extension and susceptibility/magnetization estimation of underground sources which can be obtained through the inversion procedure. It should be mentioned that the quality of the collected data and the efficiency of the inversion approach are the two critical factors to obtain a realistic model.

The EM-LIN technique has been popular due to some features, such

* Corresponding author. *E-mail address:* hghari@yazd.ac.ir (H. Ghari).

as low cost, high speed for data collection, and being non-destructive [20] and has been applied to disparate subsurface anomalies [20-22]. The EM-LIN method is categorized as a controlled source EM (CSEM) technique in the frequency domain (FD) and is widely used to investigate the conductivity distribution of near-surface structures [20-22]. The EM-LIN method is classified into three approaches based on the transmitter-receiver (Tx-Rx) distance: I) EM-38, II) EM-31, and III) EM-34, so that each Tx-Rx distance is associated with a given frequency that may be found in Table 1. In addition, Table 1 includes the effective depth of explorations in 1D mediums for the EM-LIN techniques, expressing that the exploration depth of the vertical magnetic dipoles (VMD) is two times that of the horizontal magnetic dipoles (HMD) [23]. In contrast to the magnetometry method, inversion is required for the Electromagnetic (EM) data interpretation, because there is no alternative approach for the quantitative interpretation of the EM techniques (e.g., EM34 and time domain EM).

Table 1. The EM-LIN approaches and the effective depth of exploration in 1-D environments [24].

Effective Depth of Exploration (m)				
Instrument	T-R separation (m)	Frequency (kHz)	HMD	VMD
EM-38	1	14.6	0.75	1.5
EM-31	3.66	9.8	2.75	5.50
	10	6.4	7.5	15
EM-34	20	1.6	15	30
	40	0.4	30	60

In this paper, the measured magnetic and EM34 data along a profile in the Morgenzon Farm in South Africa are utilized to discover a dolerite dyke which is the main signature of the presence of groundwater in the area. Therefore, both data sets are inverted to obtain susceptibility and conductivity distributions of the subsurface, allowing the joint interpretation of the involved methods. In our knowledge, the joint interpretation of EM-LIN data and magnetometry approaches has never been reported in literature. In addition, this case study, including these data sets, has not been investigated before.

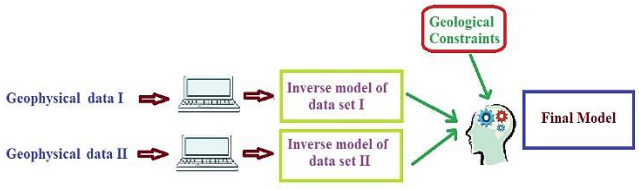

Figure 1. The illustration of geophysical data integration as joint interpretation.

2. Methodology

2.1. Forward problems of the magnetometry and EM-LIN methods

Magnetometry modelling problem has the form of a Fredholm integral equation of the first kind [8], which means that there is a linear relationship between measured magnetic data and model parameters (susceptibility/magnetization). The magnetometry inverse problem is non-unique and instable; therefore, regularization incorporating a priori information (e.g., initial model or geological information) and inserting constraints (e.g., smoothness matrix or depth weighting) are mandatory to obviate these problems. The forward problem of magnetometry may be defined as the following matrix equation:

$$\boldsymbol{d}_M = \boldsymbol{A}_M \boldsymbol{m}_M \quad (1)$$

where $\boldsymbol{d}_M$ and $\boldsymbol{m}_M$ are measured data and model parameter vectors, respectively, and $\boldsymbol{A}_M$ refers to forward operator.

Modelling problems of Electromagnetic approaches are nonlinear ones because Maxwell's equations are nonlinear with respect to conductivity. However, the EM-LIN, similar to the magnetometry method, is also a Fredholm integral equation of the first kind [22] as measured data (apparent conductivities) is linearly related to model parameters (conductivities). In fact, Perez-Flores et al. [26] took the advantage of born approximation to introduce an integral equation demonstrating a linear relationship between data and model. Again, similar to magnetometry, the EM-LIN forward modelling may be expressed simply as:

$$\boldsymbol{d}_{EM} = \boldsymbol{A}_{EM} \boldsymbol{m}_{EM} \quad (2)$$

$\boldsymbol{d}_{EM}$ and $\boldsymbol{m}_{EM}$ stands for the vectors of apparent conductivities and conductivities, respectively, and $\boldsymbol{A}_{EM}$ denotes forward operator.

Required formula for forward modelling of both methods are presented in Appendix *A*.

2.2. Inversion

Inverse problem in geophysics requires regularization to overcome its ambiguity and instability. Indeed, the presence of a model null space causes inverse solution to be non-unique. For this reason, a widespread technique which is called minimum length solution is utilized, but it includes model weighting function and zeroth order Tikhonov regularization. Since the inversion of both data sets are linear, the following objective function is minimized [26]:

$$\min \rightarrow \|\boldsymbol{W}_d(\boldsymbol{A}\boldsymbol{m} - \boldsymbol{d})\|_2^2 + \alpha \|\boldsymbol{W}_m(\boldsymbol{m} - \boldsymbol{m}_a)\|_2^2 \quad (3)$$

where $\boldsymbol{m}_a$ is the initial model for the EM-LIN method, while it is a reference model for magnetometry, α denotes regularization parameter, and $\boldsymbol{W}_d$ and $\boldsymbol{W}_m$ refer to data and model weighting matrices, respectively. Solving equation (3) can lead to the following damped weighted minimum length solution [20, 22]:

$$\boldsymbol{m} = \boldsymbol{m}_a + (\boldsymbol{W}_m^{-1}\boldsymbol{A}^T)(\boldsymbol{A}\boldsymbol{W}_m^{-1}\boldsymbol{A}^T + \alpha \boldsymbol{W}_d)^{-1}(\boldsymbol{d} - \boldsymbol{A}\boldsymbol{m}_a) \quad (4)$$

Model weighting matrix $\boldsymbol{W}_m$ is defined as:

I) For EM-LIN data: $\boldsymbol{W}_m = {}^1/_{\boldsymbol{Z}^\beta}$ (28), $\boldsymbol{Z}$ is vector of z coordinates of prism centers and β is depth weighting exponent.

II) For Magnetic data: $\boldsymbol{W}_m = \frac{1}{\boldsymbol{Z}^\beta} \frac{1}{(\boldsymbol{m}+eps)^2}$ (29), i.e. product of depth weighting and compactness constrains where $\boldsymbol{m}$ is the inverse model.

The inverse algorithm is iterative and it starts with the depth weighing function as the model weighting function for both approaches, but:

I) For the EM-LIN data inversion, the inverse model is obtained from equation (4) and is considered as the initial model for next iteration. So, the model weighing function does not update during this iterative process.

II) For magnetometry, the inverse model is used to calculate compactness function and consequently the model weighting function is updated for next iteration.

This iterative inversion procedure is continued until the maximum number of iterations (NIT) or an acceptable RMS misfit error (%) is achieved. The flowchart of the introduced algorithm is displayed in figure 2.

Regularization parameter and depth weighting exponent are two main parameters which are decisive for the inverse solution. α may be estimated from well-known techniques, such as L-curve and generalized cross validation (GCV). Parameter β has been long investigated for magnetic and gravity data inversions, but it has not been extensively examined for the inversion of EM-LIN data. In this article, β=1 is used for the inversion of both methods, because: I) for magnetometry, according to the technique presented by Cella and Fedi [19], 1 should be considered for the dyke case, and II) for the EM-LIN, the suggested value is β=1 [22 and 23].

3. Field data

South Africa's average rainfall is about 464 mm/a which is much lower

than the world average of 860 mm/a, so it is a semi-arid country. As a result of surface water scarcity, groundwater plays a critical role in water reserve for domestic, industrial, agricultural, and mining users [23]. Geophysical methods play an essential role in groundwater exploration to gain insight into subsurface geological structures that may reduce the risk of unsuccessful drilling boreholes.

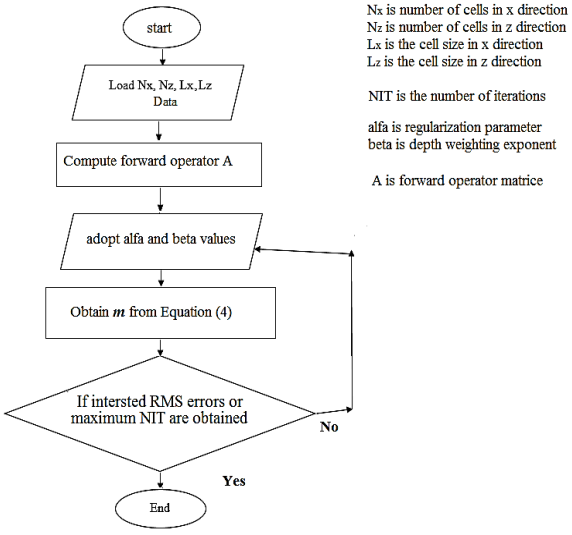

Figure 2. The flowchart of the introduced inverse algorithm.

In this section, first, the geology of the interested area is described briefly. Then, inverse models of magnetic and EM-LIN data are obtained to detect the dolerite dyke which are indicative of the presence of promising groundwater.

3.1. Geology of the study area

The geology map of the study area, i.e., the Karoo Supergroup, is displayed in figure 3A. The Karoo Supergroup (Fig. 3B) is the most well-known stratigraphic unit in South Africa which is divided into a few groups: Dwyka, Ecca, Beaufort, and Stormberg groups [31]. The Drakensberg is the youngest stratigraphic unit in the Karoo Supergroup that is composed of removed basaltic lavas. Contact planes between different strata of the Karoo rocks are desirable positions for fracture developments [30]. In the Karoo Supergroup, dolerite dykes and sills are often the principal targets for groundwater exploration [30]. Because of the high pressures and temperatures, present during the emplacement of these structures, the sedimentary host rocks along the margins of the intrusive structures are typically strongly altered [30]. These altered zones are often heavily fractured and serve as preferential pathways for groundwater movements in the Karoo [32]. Since the magnetization and resistivity contrasts of dolerite dykes (sills) are considerably larger than surrounding sedimentary materials, magnetometry and EM34 methods may be helpful to detect them.

The EM34 and magnetic data were collected along a profile with a length of 400 m. The data sets associated with each configuration of the EM34 method consisted of 40 data with a sample interval of 10m and a transmitter- receiver (T-R) separation equal to 20m. The sample interval of magnetic data, including 250 stations, was not same but they were less than 2 m.

3.2. Joint interpretation based on recovered susceptibility and conductivity models

Inversion models derived from both EM34 and magnetometry data through the regularized weighted minimum length solution algorithm are displayed in figures 4 and 5, respectively. Conductivity models retrieved from the EM34 data for both configurations are demonstrating a conductive dyke in the middle of the profile which its depth range is from less than 5m to depths of about 15m. It should be mentioned that thickness of dyke model recovered by the HMD configuration is relatively greater than the dyke reconstructed by the VMD. In addition, the conductivity model associated with the HMD has a significantly higher resolution and is also less noisy. Since both conductivity sections indicate approximately the same anomaly, we did not use the joint inversion of both configurations which can solve serious ambiguities about the conductivity distribution of the subsurface structure depending on the case. Another issue about their joint inversion is that this task should be done under the definition of an appropriate objective function allowing both configurations to have the same chance in generating the final joint model; otherwise, the final result will be dominated by one of the involving EM34 arrays. In other words, the joint model will be biased toward the individual inversion of one of them. The same problem has been reported about the combination of DC resistivity arrays [33].

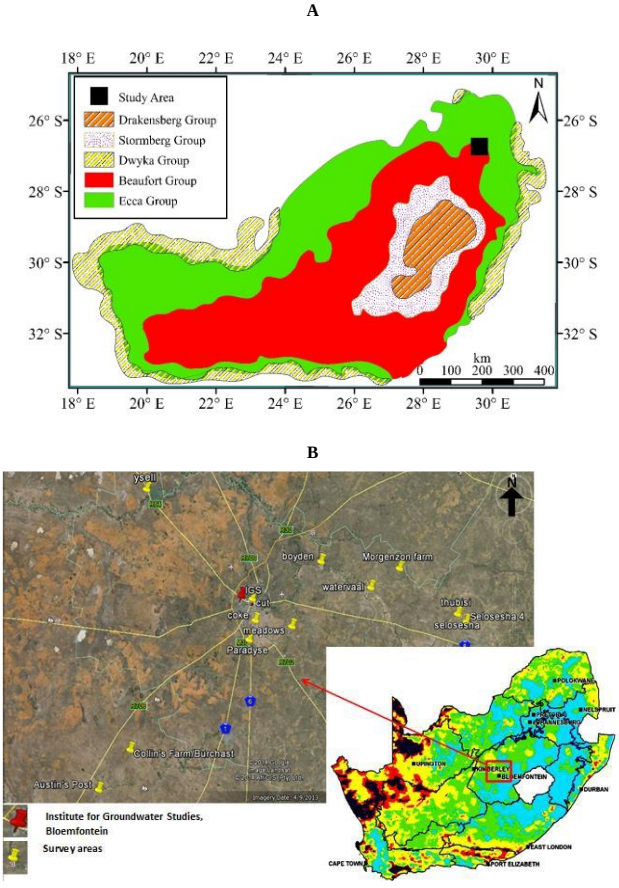

Figure 3. (A) The Geological map of the study area [34], (B) The map of the study area in South Africa [30]. The Morgenzon Farm is in the Eastern-North of the map.

The susceptibility model recovered from the magnetic data (figure 5), similar to the EM34 method, is representing a dolerite dyke in the middle of the profile which is extended from near surface to depths more than 15 m. The dyke is relatively thinner than dykes obtained from the EM34 arrays, but the susceptibility section has substantial better resolution. Furthermore, the susceptibility section is not noisy which clearly expresses an anomaly with significant susceptibility / magnetization contrast with its non-magnetized surrounding background. The computed data versus measured data for both methods are shown in figure 6. Adopted regularization parameters, depth weighting exponents, NITs, and RMS misfit values for both methods are presented in table 2.

Finally, from the joint interpretation process, it may be concluded

that the correlation of EM34 models and the magnetic susceptibility model indicates a dolerite dyke model in the middle of the profile with a depth range from less than 5 to 15m.

Table 2. The values of inversion parameters for the gravimetry and magnetometry data inversion.

data	α	β	NITs	misfit error (%)
EM-LIN (HMD)	0.0045	1	4	2.78
EM-LIN (VMD)	0.0434	1	4	6.23
Magnetometry	3831.3	1	4	5.43

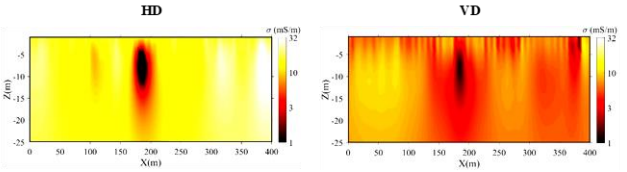

Figure 4. The reconstructed inverse models from the EM34 data for both HMD and VMD configurations.

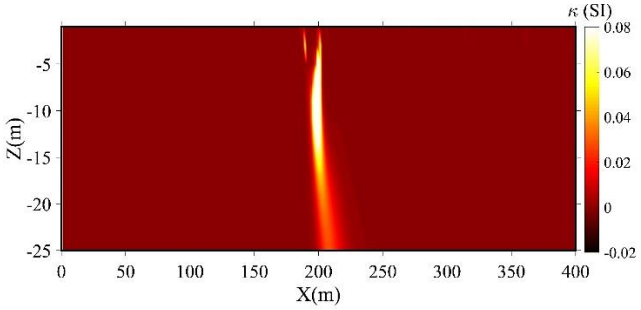

Figure 5. The inversion model derived from the magnetometry data.

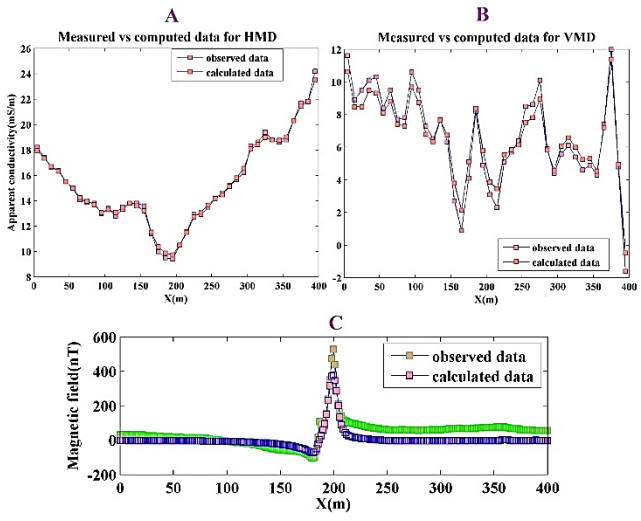

Figure 6. The computed data vs measured data for the A) EM34 (HMD), B) EM34 (VMD), and C) magnetic methods.

4. Conclusion

The joint interpretation of geophysical approaches, such as EM34 and magnetometry, can be useful especially when they show a high correlation about the interested underground anomalies. In this paper, the EM34 and magnetic methods were used to detect a dolerite dyke as the signature of groundwater presence in the Morgenzon Farm in South Africa. Due to the notable difference in the susceptibility and conductivity contrasts of the dolerite dyke with surrounding sedimentary materials, conductivity-based methods, including EM34 and magnetic approaches may lead to desired results. The inverse problems of both methods are Fredholm integral equation of the first kind which means that we are faced with linear inversion. So, the regularized weighted minimum length solution algorithm was used to reveal the susceptibility and conductivity distribution of the subsurface. The model weighting matrix was the product of depth weighting and compactness constraints for magnetometry, while the depth weighting is employed as the model weighting for the EM34. Reconstructed models from both data sets show a high degree of consistency and their correlation is representative of a dyke in the middle of the study profile which is extended from 4 to 15m vertically. Finally, the inversion models derived from the EM34 configurations are much noisier than the susceptibility section, because the susceptibility of surrounding sedimentary rocks is close to zero, while this is not true about the conductivity distribution of subsurface.

Acknowledgements

We acknowledge Ms. Makhokha from University of the Free State for giving us access to the data.

REFERENCES

[1] Orlando, L., 2005. Joint interpretation of geophysical data for archaeology. A case study. Subsurface Sensing Technologies and Applications, 6(2), 235-250.

[2] Al Farajat, M. (2009). Characterization of a coastal aquifer basin using gravity and resistivity methods: a case study from Aqaba in Jordan. *Acta Geophysica*, *57*(2), 454-475.

[3] Sultan, S. A., Santos, F. A. M., & Abbas, A. M. (2010). Joint inversion interpretation for gravity and resistivity data: a case study at New Heliopolis City, Cairo, Egypt. *Near Surface Geophysics*, *8*(1), 43-53.

[4] Karavul, C., Dedebali, Z., Keskinsezer, A., Demirkol, A., 2010. Magnetic and electrical resistivity image survey in a buried Adramytteion ancient city in Western Anatolia, Turkey. International Journal of Physical Sciences, 5(6), 876-883.

[5] Gambetta, M., Armadillo, E., Carmisciano, C., Stefanelli, P., Cocchi, L., & Tontini, F. C. (2011). Determining geophysical properties of a near-surface cave through integrated microgravity vertical gradient and electrical resistivity tomography measurements. *Journal of cave and karst studies*, *73*(1), 11-15.

[6] Zhang, G., Lu, Q.T., Zhang, G.B., 2018. Joint Interpretation of Geological, Magnetic, AMT, and ERT Data for Mineral Exploration in the Northeast of Inner Mongolia, China. Pure and Applied Geophysics, 175(3), 989-1002.

[7] Ebrahimi, A., Dehghan, M. J., & Ashtari, A. (2019). Contribution of gravity and Bristow methods for Karez (aqueduct) detection. *Journal of Applied Geophysics*, *161*, 37-44.

[8] Ghanati R., Ghari, H.A., Mirzaei M., Hafizi M.K. (2015). Nonlinear inverse modeling of magnetic anomalies due to thin sheets and cylinders using Occam's method. In*: 8th congress of the Balkan geophysical society, Chania, Greece*. doi: https://doi.org/10.3997/2214-4609.201414178

[9] Urban, T.M., Rasic, J.T., Alix, C., Anderson, D.D., Chisholm, L., Jacob, R.W., Manning, S.W., Mason, O.K., Tremayne, A.H. & Vinson, D. (2019). Magnetic detection of archaeological hearths in Alaska: A tool for investigating the full span of human

presence at the gateway to North America. *Quaternary Science Reviews*, 211, 73-92. doi: https://doi.org/ 10.1016/ j.quascirev.2019.03.018.

[10] Al-Farhan, M., Oskooi, B., Ardestani, V. E., Abedi, M., & Al-Khalidy, A. (2019). Magnetic and gravity signatures of the Kifl oil field in Iraq. *Journal of Petroleum Science and Engineering*, 183, 106397. doi: https://doi.org/10.1016/j.petrol.2019.106397.

[11] Fedi, M., La Manna, M., & Palmieri, F. (2003). Nonstationary analysis of geomagnetic time sequences from Mount Etna and North Palm Springs earthquake. *Journal of Geophysical Research: Solid Earth*, 108 (B10). doi: https://doi.org/ 10.1029/2001JB000820.

[12] Caratori Tontini, F., De Ronde, C. E. J., Yoerger, D., Kinsey, J., & Tivey, M. (2012). 3-D focused inversion of near-seafloor magnetic data with application to the Brothers volcano hydrothermal system, Southern Pacific Ocean, New Zealand. *Journal of Geophysical Research: Solid Earth*, 117(B10). doi: https://doi.org/10.1029/2012JB009349

[13] Al-Garni, M. (2011). Magnetic and DC resistivity investigation for groundwater in a complex subsurface terrain. *Arabian Journal of Geosciences*, *volume,* 4, 385–400. doi: https:// doi.org/10.1007/s12517-009-0071-z.

[14] Ghari, H., Varfinezhad, R., & Parnow, S. (2023). 3D joint interpretation of potential field, geology, and well data to evaluate a salt dome in the Qarah-Aghaje area, Zanjan, NW Iran. *Near Surface Geophysics*, 21(3), 233-246. doi: https:// doi.org/10.1002/nsg.12252.

[15] Fedi, M. (2007). DEXP: A fast method to determine the depth and the structural index of potential fields sources. *Geophysics*, 72 (1), I1-I11. doi: https://doi.org/10.1190/1.2399452.

[16] Fedi, M., & Pilkington, M. (2012). Understanding imaging methods for potential field data. *Geophysics*, 77 (1), G13-G24. doi: https://doi.org/10.1190/geo2011-0078.1.

[17] Mehrvash, M., Abedi, M., Norouzi, G. H. (2023). A potential field geophysical study to image a Potash resource through Depth from Extreme Points, Ghareh-Aghaj deposit in NW of Iran. *International Journal of Mining and Geo-Engineering,* 57(3), 241-250. doi: https://doi.org/10.22059/ijmge.2023.354047.595024.

[18] Pilkington, M. (2009). 3D magnetic data-space inversion with sparseness constraints. *Geophysics*, 74(1), L7-L15. doi: https://doi.org/10.1190/1.3026538.

[19] Cella, F., & Fedi, M. (2012). Inversion of potential field data using the structural index as weighting function rate decay. *Geophysical Prospecting*, *60* (2), 313-336. doi: https:// doi.org/ 10.1111/j.1365-2478.2011.00974.x.

[20] Parnow, S., Oskooi, B., & Florio, G. (2021). Improved linear inversion of low induction number electromagnetic data. *Geophysical Journal International*, 224(3), 1505-1522. doi: https://doi.org/10.1093/gji/ggaa531

[21] Pérez-Flores, M. A., Antonio-Carpio, R. G., Gómez-Treviño, E., Ferguson, I., & Méndez-Delgado, S. (2012). Imaging of 3D electromagnetic data at low-induction numbers. *Geophysics*, 77(4), WB47-WB57. doi: https://doi.org/10.1190/geo2011-0368.1

[22] Ghari, H., & Varfinezhad, R. (2022). 2D Linear inversion of ground-based controlled-source electromagnetic data under a low induction number condition. *Journal of the Earth and Space Physics*, 48(3), 557-573. doi: https://doi.org/10.22059/ jesphys.2022.334600.1007385.

[23] Varfinezhad, R., & Parnow, S. (2022). 3D Electromagnetic low induction number modeling using integral equations. *Journal of the Earth and Space Physics*, *47*(4), 99-110. doi: https://doi.org/ 10.22059/jesphys.2021.325291.1007330.

[24] McNeill, J. D. (1980). Electromagnetic terrain conductivity measurement at low induction numbers.

[25] Gallardo, L.A. (2004). Joint two-dimensional inversion of geoelectromagnetic and seismic refraction data with cross-gradients constraint (Doctoral dissertation, University of Lancaster).

[26] Pérez-Flores, M. A., Méndez-Delgado, S., & Gómez-Treviño, E. (2001). Imaging low-frequency and dc electromagnetic fields using a simple linear approximation. *Geophysics*, 66(4), 1067-1081. Doi: https://doi.org/10.1190/1.1487054.

[27] Tikhonov, A. N., & Arsenin, V. I. A. K. (1977). Solutions of ill-posed problems.

[28] Li, Y., & Oldenburg, D. W. (1996). 3-D inversion of magnetic data. *Geophysics*, 61(2), 394-408. doi: https:// doi.org/ 10.1190/1.1443968

[29] Last, B. J., & Kubik, K. (1983). Compact gravity inversion. *Geophysics*, 48(6), 713-721. doi: https://doi.org/10.1190/1.1441501.

[30] Makhokha, D., & Fourie, F. (2016). A systematic approach to the interpretation of conductivity anomalies across intrusive dolerite dykes and sills in the Karoo Supergroup (Doctoral dissertation, MSc thesis. University of the Free State, Bloemfontein).

[31] Geel, C., 2014. Brief geologic overview of the Cape Fold Belt and Karoo Basin: Field excursion to Matjiesfontein, 10th Inkaba yeAfrica conference. Matjiesfontein, Inkba yeAfrica.

[32] Duncan, R. A., Hooper, P. R., Rehacek, J., Marsh, J., & Duncan, A. R. (1997). The timing and duration of the Karoo igneous event, southern Gondwana. *Journal of Geophysical Research: Solid Earth*, *102*(B8), 18127-18138. doi: https://doi.org/ 10.1029/ 97JB00972.

[33] Athanasiou, E. N., Tsourlos, P. I., Papazachos, C. B., & Tsokas, G. N. (2007). Combined weighted inversion of electrical resistivity data arising from different array types. *Journal of applied geophysics*, *62*(2), 124-140. doi: https://doi.org/10.1016/ j.jappgeo.2006.09.003.

[34] De Kock, M.O., Beukes, N.J., Götz, A.E., Cole, D., Robey, K., Birch, A., Withers, A. & Van Niekerk, H.S. (2016). Open file progress report on exploration of the Southern Karoo Basin through CIMERAKARIN borehole KZF-1 in the Tankwa Karoo, Witzenberg (Ceres) district. DST-NRF Centre of Excellence for Integrated Mineral and Energy Resources Analysis (CIMERA), *University of Johannesburg, South Africa*.

[35] Blakely, R. J. (1996). *Potential theory in gravity and magnetic applications*. Cambridge university press.

[36] Vatankhah, S., Ardestani, V. E., & Renaut, R. A. (2014). Automatic estimation of the regularization parameter in 2D focusing gravity inversion: application of the method to the Safo manganese mine in the northwest of Iran. *Journal of Geophysics and Engineering*, *11*(4), 045001. https://doi.org/10.1088/1742-2132/11/4/045001

Appendix A

A.1. The forward modelling of magnetometry

The subsurface of the study area is divided into a large number of cells with rectangular cross- sections for which susceptibility within each cell is considered constant (such as figure (A-1)). For the forward problem, the model vector, including susceptibilities is known and we want to compute the data vector, i.e., the magnetic anomaly. In order to calculate forward response of a magnetic source, the following equation may be used [35]:

$$d_i = \sum_{j=1}^{M}\sum_{k=1}^{4}(\hat{f}_x B_x^l + \hat{f}_z B_z^l)_i \quad \text{(A-1)}$$

where d_i denotes the predicted magnetic response at the ith point, $\hat{f}_x$ and $\hat{f}_z$ refer to the unit components corresponding to the geomagnetic field along x and z axes, B_x^l and B_z^l express the horizontal and vertical components of the magnetic field, respectively, associated with ribbons as equations (A-2) and (A-3):

$$B_x = -2C_m(M.\hat{n})[\hat{s}_x \log\left(\frac{r_2}{r_1}\right) - \hat{s}_z(\theta_1 - \theta_2)] \quad \text{(A-2)}$$

$$B_z = -2C_m(M.\hat{n})[\hat{s}_z \log\left(\frac{r_2}{r_1}\right) + \hat{s}_x(\theta_1 - \theta_2)] \quad \text{(A-3)}$$

r_1, r_2, θ_1 and θ_2 are shown in figure (A-1), $\hat{n}$ stands for the unit vector which is vertical to each cell, $\hat{s}_x = -\widehat{n_z}$, $\hat{s}_z = -\widehat{n_x}$ and $C_m = \frac{\mu_0}{4\pi} = 10^{-7}$ in the SI units.

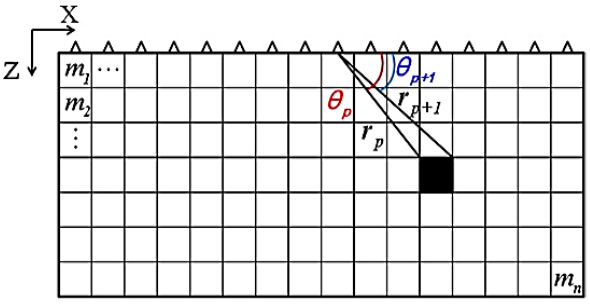

Figure A-1. The discretizing subsurface into a lot of cells with square or rectangular cross-sections [36].

Equation (A-1) may be simply written as matrix equation (A-4):

$$\mathbf{A}\boldsymbol{m}=\boldsymbol{d} \quad \text{(A-4)}$$

where A is forward operator matrix and $\boldsymbol{m}$ and $\boldsymbol{d}$ express the vectors of model parameters and observed magnetic anomaly, respectively.

A.2. The forward modelling of the EM-LIN

Perez-Flores et. al [26] introduced the linear integral equations (IEs) approach for the 3D EM-LIN modelling of horizontal and vertical magnetic dipoles using the Born approximation. These IEs are Fredholm Integral equation of the first kind for which observed apparent conductivities are linearly related to the true conductivities as the following equations for vertical magnetic dipoles (VMD):

$$\sigma_a(r_1, r_2) = -\frac{16\pi s}{\omega\mu_0 m_z}\iint_v^{\square} G_{Hz}(r, r_2).E_{Hz}(r, r_1)\sigma(r)d^3r \quad \text{(A-5)}$$

and for horizontal magnetic dipoles (HMD):

$$\sigma_a(r_1, r_2) = -\frac{16\pi s}{\omega\mu_0 m_y}\iint_v^{\square} G_{Hy}(r, r_2).E_{Hy}(r, r_1)\sigma(r)d^3r \quad \text{(A-6)}$$

where s, ω and μ_0 stand in turn for T-R separation, angular frequency, and magnetic permeability, while m_z and m_y are magnetic momentums around z and y direction, respectively. σ_a and $\sigma(r)$ express observed apparent conductivity and conductivity distribution of the subsurface. r_1, r_2 and r represent position vectors of the transmitter, receiver, and subsurface model, respectively (figure A-2). Associated expressions of $G_{Hz}(r, r_2)$, $G_{Hy}(r, r_2)$, $E_{Hz}(r, r_1)$ and $E_{Hy}(r, r_1)$ can be found in Table (A-1).

Table A-1. The Dyadic Green's function [2].

$G_{H_z}(r, r_2) = \frac{1}{4\pi}\left[-\frac{(y-y_2)}{\lvert r-r_2\rvert^3}i + \frac{(x-x_2)}{\lvert r-r_2\rvert^3}j\right]$
$E_{H_z}(r, r_1) = \frac{\omega\mu_0 m_z}{4\pi}\left[-\frac{(y-y_1)}{\lvert r-r_1\rvert^3}i + \frac{(x-x_1)}{\lvert r-r_1\rvert^3}j\right]$
$G_{H_y}(r, r_2) = \frac{1}{4\pi}\left\{\left[\frac{1}{\rho_2^2} - \frac{z+h}{\rho_2^2\lvert r-r_2\rvert} - \frac{2(y-y_2)^2}{\rho_2^4} + \frac{2(z+h)(y-y_2)^2}{\rho_2^4\lvert r-r_2\rvert} + \frac{(z+h)(y-y_2)^2}{\rho_2^2\lvert r-r_2\rvert^3}\right]i + \left[\frac{(x-x_2)(y-y_2)}{\rho_2^2}\left(\frac{2}{\rho_2^2} - \frac{2(z+h)}{\rho_2^2\lvert r-r_2\rvert} - \frac{z+h}{\lvert r-r_2\rvert^3}\right)\right]j\right\}$
$E_{H_y}(r, r_2) = \frac{\omega\mu_0 m_y}{4\pi}\left\{\left[\frac{1}{\rho_1^2} - \frac{z+h}{\rho_1^2\lvert r-r_1\rvert} - \frac{2(y-y_1)^2}{\rho_1^4} + \frac{2(z+h)(y-y_1)^2}{\rho_1^4\lvert r-r_1\rvert} + \frac{(z+h)(y-y_1)^2}{\rho_1^2\lvert r-r_1\rvert^3}\right]i + \left[\frac{(x-x_1)(y-y_1)}{\rho_1^2}\left(\frac{2}{\rho_1^2} - \frac{2(z+h)}{\rho_1^2\lvert r-r_1\rvert} - \frac{z+h}{\lvert r-r_1\rvert^3}\right)\right]j\right\}$

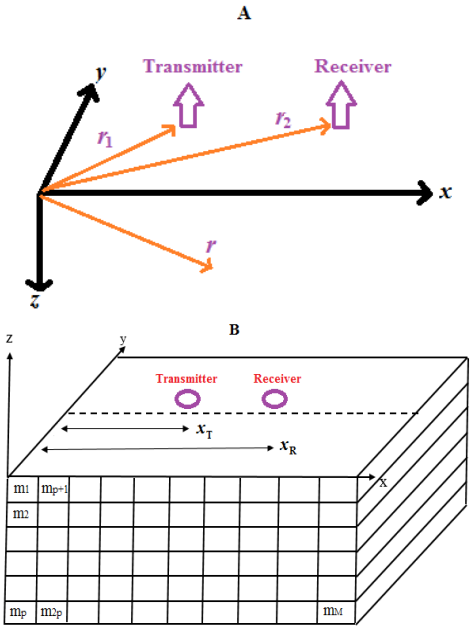

Figure A-2. (A) The representation of transmitter, receiver, and subsurface position vectors. (B) Discretizing subsurface into a lot of prismatic cells which have infinite lengths along the y-direction.

To obtain appropriate expressions for the corresponding 2D problem, we integrate equations (A-5) and (A-6) from minus infinity to infinity along the y-axis (strike direction), which can be done analytically or numerically. In this paper, the numerical integration is performed to achieve the 2D case. The subsurface is discretized into $n_x \times n_z$ prisms with side lengths of lx and lz, which extend infinitely along the y-direction (figure A-2B). The integration of equations (A-5) and (A-6) along the y-axis must be carried out according to the following formulas:

$$\sigma_{a,V} = -\frac{16\pi s}{\omega\mu_0 m_z}\iint_{\square}\left\{\int_{-\infty}^{\infty} G_{H_z}(r, r_2).E_{Hz}(r, r_1)\sigma(r)dy\right\}dxdz \quad \text{(A-7)}$$

and

$$\sigma_{a,H} = -\frac{16\pi s}{\omega\mu_0 m_y}\iint_{\square}\left\{\int_{-\infty}^{\infty} G_{H_y}(r, r_2).E_{Hy}(r, r_1)\sigma(r)dy\right\}dxdz \quad \text{(A-8)}$$

Therefore, by implementing numerical integration along the y-axis and discretized equations (A-7) and (A-8) along with x and z directions, we may again form the following matrix equations for each configuration of magnetic dipoles:

$$\mathbf{d}=\mathbf{Am} \quad \text{(A-9)}$$

where $\mathbf{d}$ is the vector of measured apparent conductivities, $\mathbf{m}$ contains unknowns (model parameters), and $\mathbf{A}$ is the kernel matrix or forward operator.